Stochastic characterization of multiscale material uncertainties on the fibre-matrix interface stress state of composite variable stiffness plates

International Journal of Engineering Science 183 (2023) 103787

Contents lists available at ScienceDirect

International Journal of Engineering Science

journal homepage: www.elsevier.com/locate/ijengsci

# Stochastic characterization of multiscale material uncertainties on the fibre-matrix interface stress state of composite variable stiffness plates

A. Pagani *, M. Petrolo, A.R. Sánchez-Majano

*MUL2 Lab, Department of Mechanical and Aerospace Engineering, Politecnico di Torino, Corso Duca degli Abruzzi 24, 10129 Torino, Italy*

ARTICLE INFO

*Keywords:*
VAT composites
Multiscale
Defect modelling
Uncertainty analysis
CUF

ABSTRACT

This work analyses the stochastic response of fibre and matrix scale stresses of Variable Angle Tow (VAT) laminates affected by multiscale uncertainty defects. The aim is to evaluate the influence of the innermost constituents on the overall structural response via an accurate mechanical characterization of both macro- and microscales. The Carrera Unified Formulation (CUF) is employed to obtain two-dimensional (2D) and one-dimensional (1D) models for both scales. Indeed, 2D layer-wise (LW) and 1D component-wise (CW) approaches are adopted for the macroscale and the microscale, respectively. The use of 2D and 1D models proves to be convenient as a superior computational efficiency is reached, this aspect being of great importance as many analyses are necessary for uncertainty quantification. The numerical results demonstrate the validity of the proposed methodology to obtain an accurate description of the 3D stress state at the different scales. A special focus is made on the fibre-scale stresses and how they may vary when affected by multiscale uncertainty.

## 1. Introduction

Due to favourable trade-offs between mechanical properties and weight, composite materials are currently employed in many applications, e.g., aerospace, automotive, naval, and wind energy structures. However, knowledge gaps exist in predicting various mechanical phenomena, such as failure onset and progression. One of the complicating features of composites is their hierarchic nature, as various scales play a role in the structural problem. Due to their enormous computational cost, direct numerical simulations of all scales are not carried out. Instead, multiscale modelling approaches are preferred with a bottom-up transfer of information to link the innermost constituents to the macroscopic structure, as depicted in (Llorca et al., 2011).

Concerning the macroscopic level, many structural theories have been devoted to the analysis of thin structures. For instance, Poisson (Poisson, 1829), Mindlin Mindlin (1951), Kirchhoff (Kirchhoff, 1850), Reissner (Reissner, 1945) and Cauchy (Cauchy, 1828) conceived the classical formulation of plate and shell models. However, their applicability is restricted to a narrow range of applications, such as thin-walled structures and without local effects. Conversely, advanced formulations are required when transverse stresses cannot be neglected. During the last decades, improved formulations have been developed to enhance the accuracy of such classical theories. As an example, Reddy (Reddy, 1984) introduced a simple high-order theory for two-dimensional (2D) laminated composite structures. Similarly, Reddy and Liu (Reddy & Liu, 1985) proposed a shear model consisting of a parabolic distribution for the through-the-thickness shear deformations. Moreover, Carrera (Carrera, 2002, 2003) developed several refined shell theories in the framework of the Carrera Unified Formulation (CUF).

* Corresponding author.
*E-mail addresses:* alfonso.pagani@polito.it (A. Pagani), marco.petrolo@polito.it (M. Petrolo), alberto.racionero@polito.it (A.R. Sánchez-Majano).

https://doi.org/10.1016/j.ijengsci.2022.103787
Received 31 August 2022; Received in revised form 26 October 2022; Accepted 26 October 2022

Micromechanical modelling methods help describe microscopic features, such as the arrangement of the fibres, volume fractions or void presence, and how they affect the global response of the homogenized material. The micromechanical research field is continuously evolving and several analytical, semi-analytical and numerical methods have been proposed over the years. An insightful review of different homogenization procedures can be found in Hassani and Hinton (1998), Nemat-Nasser and Hori (2013). Many of these methods assume that reinforcements are arranged following a regular, periodic pattern and recall the concept of Repeating Unit Cell (RUC), which establishes the minimum geometrical entity that can be periodically repeated over the space to match the higher scale structure. RUC models can be based on analytical approaches such as the rule of mixtures (Hill, 1952), the Hashin–Shtrikman (Hashin & Shtrikman, 1962) bounds or the Mori–Tanaka method (Mori & Tanaka, 1973). Other methods can be applied to solve more generic cases, such as the method of cells (Aboudi, 1989). Fully numerical methods, such as FEM, are often employed as micromechanics tools to predict the local fields within the constituent material (Heinrich et al., 2012; Sun & Vaidya, 1996). Micromechanical FEM models can also be embedded into more advanced analyses, such as the multiscale progressive damage failure of textile composites (Dang et al., 2020; Zhao, Dang, Zhang, Yun, & Li, 2018).

Thanks to new manufacturing capabilities, such as the Automated Fibre Placement (AFP), Automated Tape Laying (ATL), or Fused Deposition Modeling (FDM), novel families of laminated components have become feasible to produce, despite being conceived decades ago (DiNardo & Lagace, 1989; Leissa & Martin, 1990). An example is variable stiffness composites (VSC) or variable angle tow (VAT) composites, in which fibre tows are steered following curvilinear paths. In recent years, research efforts have aimed for a realistic characterization of these new composites. Modelling strategies have been conceived to include manufactured-induced defects. For instance, (Falcó et al., 2017, 2014) managed to insert gaps and overlaps into the numerical model and study their influence on the failure of these components. Fayazbakhsh, Nik, Pasini, and Lessard (2013) introduced Defect Layer Method (DLM) and used it to investigate the influence of shear deformation in the mechanical performance of laminated structures with curvilinear fibre paths, Akbarzadeh, Arian Nik, and Pasini (2014). Other mesoscale fabrication flaws, such as misalignment, have been studied in van den Broek, Minera, Jansen, and Rolfes (2021), focusing on the post-buckling behaviour and enhancing the structure's performance.

Manufacturing uncertainties can be modelled via stochastic fields (Ghanem & Spanos, 1991). Random fields spread a parameter over a domain and are defined by a mean value, standard deviation and correlation function. For instance, (Balokas, Kriegesmann, Czichon, & Rolfes, 2019) investigated the influence of yarn distortion and waviness on the stiffness and strength of braided composites by modelling the distortion and waviness using 1D spectral stochastic fields. 2D fields can be employed to mimic fibre waviness at the laminate scale, as in Scarth and Adhikari (Scarth & Adhikari, 2017), or variability in the material properties on curved surfaces, such as aircraft wings (Scarth, Adhikari, Cabral, Silva, & do Prado, 2019).

In this manuscript, the Carrera Unified Formulation (CUF) (Carrera, Cinefra, Petrolo, & Zappino, 2014) is utilized to generate higher-order structural models as CUF can obtain any structural theory without *ad hoc* assumptions, unlike classic theories do. Additionally, CUF has demonstrated its wide applicability in a plethora of mechanical problems, such as stress analyses of highly-flexible thin-walled structures (Pagani, Azzara, Augello, & Carrera, 2021), peridynamics (Pagani, Enea, & Carrera, 2021), microscale characterization (de Miguel, Pagani, Yu, & Carrera, 2017; Kaleel, Petrolo, Waas, & Carrera, 2017) and VAT components (Viglietti, Zappino, & Carrera, 2019). Concerning the latter, 1D and 2D models have been developed to study the influence of uncertainty defects on the mechanical performance of VSC (Pagani & Sanchez-Majano, 2020, 2021; Pagani, Sanchez-Majano, & Zarate, 2021; Sanchez-Majano, Pagani, Petrolo, & Zhang, 2021), and understand the effect of the fibre path on the linear stress response of VAT shells (Sanchez-Majano, Azzara, Pagani, & Carrera, 2021).

In this context, the present work aims to analyse the stochastic behaviour of the microscale stress state of VAT plates subjected to defects. Although microscale stress state characterization is helpful for simulating the progressive failure and delamination of composites, this manuscripts strictly restricts to the failure onset analysis. The progressive failure and delamination of composites using refined beam models in the CUF framework has already been addressed by Kaleel, Petrolo, Waas, and Carrera (2018) and Kaleel, Carrera and Petrolo (Kaleel, Carrera, & Petrolo, 2020). In this manuscript, flaws are included via stochastic fields, whereas the different scales are modelled using 1D and 2D higher-order CUF finite elements (FE) for the micro and mesoscale. Flaws only concern the material elastic properties. This paper is organized as follows: first, the FE description of the different scales is introduced in Section 2. Then, the uncertainty modelling and through-the-scale propagation are depicted in Section 3. Numerical assessments are available in Section 4 and conclusions are drawn in Section 5.

## 2. Multiscale and finite element models of VAT

### 2.1. Modelling of the macroscale

2D FE models are used within CUF. According to Carrera et al. (2014), the 3D displacement field can be expressed as a summation of arbitrary expansions of the 2D generalized unknowns laying over the $x$–$y$ plane, i.e.,

$$\mathbf{u}(x, y, z) = F_\tau(z)\mathbf{u}_\tau(x, y) \quad \tau = 1, \dots, M \tag{1}$$

$M$ is the number of expansion terms, $\mathbf{u}_\tau(x, y)$ is the vector of the generalized displacements, and $F_\tau(z)$ is the through-the-thickness expansion. Equivalent single layer (ESL) and layer-wise (LW) approaches are commonly adopted in the analysis of composite structures. In this work, ESL models are obtained using Taylor Expansion (TE), whilst LW ones rely on Lagrange Expansion (LE). The acronym TE$N$ denotes the $N$th-order TE, while LE$N$ indicates an $N$th-order LE. The differences in the assembly procedure for both ESL and LW and the behaviour of the primary variables along the plate thickness are reported in Fig. 1. In ESL, the homogenization

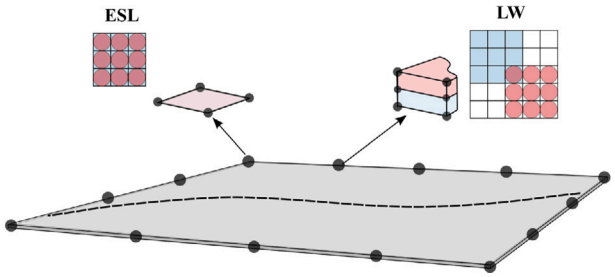


**Fig. 1.** Assembly procedures for ESL and LW models, and graphical representation of the displacement variables through the thickness of the plate.

of the properties of each layer is carried out and are summed altogether when computing the stiffness matrix. Conversely, the LW approach considers each layer independently and expands the displacement field within each lamina; consequently, the continuity of displacements has to be imposed at the interface, see Carrera (2002), Pagani, Yan, and Carrera (2017).

Using FE and shape functions $N_i(x, y)$, the displacement field becomes:

$$\mathbf{u}_\tau(x, y) = N_i(x, y)F_\tau(z)\mathbf{q}_{\tau i} \quad i = 1, \dots, N_n \tag{2}$$

$\mathbf{q}_{\tau i}$ represents the unknown nodal variables, $N_n$ indicates the number of nodes per element. 2D nine-node quadratic and sixteen-node cubic finite elements, Q9 and Q16, are employed for the shape functions in the $x$–$y$ plane.

The principle of virtual displacements (PVD) is employed to obtain the governing equations of the FE model. The PVD states that the virtual variation of the internal strain energy $\delta L_{int}$ has to be equal to the virtual work of the external forces $\delta L_{ext}$, that is:

$$\delta L_{int} = \delta L_{ext} \tag{3}$$

Therein, the virtual variation of the strain energy can be calculated as:

$$\delta L_{int} = \int_V \delta\boldsymbol{\epsilon}^T \boldsymbol{\sigma} dV \tag{4}$$

while that of the external forces reads as:

$$\delta L_{ext} = \int_V \mathbf{P} N_j F_s \delta \mathbf{u}_{sj}^T dV \tag{5}$$

in which $\mathbf{P}$ is a $3 \times 1$ array containing the external forces. $\delta L_{int}$ can be rewritten using Eqs. (2) and (4), the constitutive law $\boldsymbol{\sigma} = \bar{\boldsymbol{C}}\varepsilon$ and the geometrical relations between strains and displacements, which yields:

$$\delta L_{int} = \delta \mathbf{q}_{sj}^T \mathbf{k}^{ij\tau s} \mathbf{q}_{\tau i} \tag{6}$$

where $\mathbf{k}^{ij\tau s}$ is the $3 \times 3$ Fundamental Nucleus (FN), which remains constant regardless of the order 2D shape functions and through-the-thickness expansion, as shown in Carrera et al. (2014). The mathematical expression for the FN results in:

$$\mathbf{k}^{ij\tau s} = \int_V \mathbf{D}^T (N_j F_s) \bar{\mathbf{C}} \mathbf{D} (N_i F_\tau) dV \tag{7}$$

in which $\mathbf{D}$ is the differential operator containing the geometrical relations between strains and displacements, $\bar{\mathbf{C}}$ is the material stiffness matrix in the global reference system, that is, $\bar{\mathbf{C}} = \mathbf{T}(x, y)^T \mathbf{C} \mathbf{T}(x, y)$. Finally, the global assembled stiffness matrix $\mathbf{K}$ is obtained by looping through the indices $i$, $j$, $\tau$ and $s$.

### 2.2. Microscale models

Microscale analyses of composite structures exploit a series of microstructures periodically distributed throughout the volume, i.e., the Representative Unit Cell (RUC), containing the necessary information to identify the material properties. A graphical description of a RUC is available in Fig. 2. The macroscopic properties can be identified in the global reference system $\mathbf{x} = \{x_1, x_2, x_3\}$, whereas RUC's local reference is identified by $\mathbf{y} = \{y_1, y_2, y_3\}$. Micromechanical analyses assume that the RUC is much smaller than the macroscopic structure, such that $\mathbf{y} = \mathbf{x}/\delta$, where $\delta$ is the characteristic length of the RUC and acts as a scaling factor. In micromechanics, the material properties provided by the RUC analysis at the microscale do not depend on the macroscale structural problem, i.e., they are intrinsic properties of the material chosen for the structural analysis. Furthermore, the global solution of the macroscopic problem is equal to the local solution over the RUC volume. For instance, for a generic field $\phi(\mathbf{x}; \mathbf{y})$,

$$\bar{\phi}(\mathbf{x}) = \frac{1}{V} \int_V \phi(\mathbf{x}; \mathbf{y}) dV \tag{8}$$

$V$ is the volume of the RUC, $\phi(\mathbf{x}; \mathbf{y})$ is the local field, depending on the global and local coordinates, and $\bar{\phi}$ is the average field, depending only on the global coordinates. In addition, periodic boundary conditions are commonly imposed to guarantee the

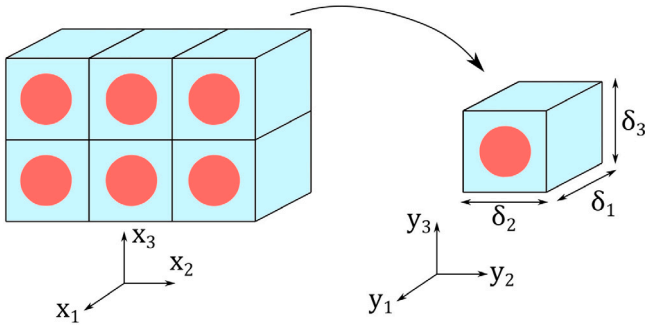


**Fig. 2.** Periodically distributed microstructures and RUC.

compatibility of deformations for the adjacent RUC. The micromechanical analyses shown in this work employ the Variational Asymptotic Method (VAM) (Yu, Hodges, & Ho, 2012) and Mechanics of Structure Genome (MSG) (Yu & Tang, 2007). These are coupled with CUF to (i) calculate the homogenized properties of the heterogeneous material and use them for the macroscale analysis; (ii) retrieve the microscale stress state. According to MSG, the properties of an RUC can be calculated by minimizing the difference between the strain energies of the heterogeneous structure and the equivalent homogeneous material, as described by the following functional:

$$\Pi = \frac{1}{V}\int_V \frac{1}{2} C_{ijkl}\varepsilon_{ij}\varepsilon_{kl} dV - \frac{1}{2} C^*_{ijkl}\bar{\varepsilon}_{ij}\bar{\varepsilon}_{kl} \tag{9}$$

The first term denotes the strain energy of the heterogeneous material represented by the RUC, and the second corresponds to the strain energy of the homogeneous one. Therein, $C_{ijkl}$ denotes the fourth-order elastic tensor, and $\varepsilon_{ij}$ is the second-order strain tensor. Similarly, $C^*_{ijkl}$ and $\bar{\varepsilon}_{ij}$ are their counterparts in the homogeneous material. For the sake of brevity, the derivation of the equations that lead to minimizing the functional is omitted, but it can be found in de Miguel et al. (2017), Yu (2016), Yu and Tang (2007). Finally, the functional is written as:

$$\Pi = \frac{1}{2}\int_V C_{ijkl}(\bar{\varepsilon}_{ij} + \chi_{i,j})(\bar{\varepsilon}_{kl} + \chi_{k,l}) dV \tag{10}$$

$\chi_{i,j}$ is the derivative of the fluctuation $\chi_i$. The MSG equations are solved using 1D CUF models. As illustrated in Fig. 2, the longitudinal axis coincides with $y_1$ and the fibre direction, whilst the fibre-matrix phases lie on the $y_2 - y_3$ plane. Fluctuations $\chi$ can be expanded over the cross-section by using arbitrary functions depending on the $y_2$ and $y_3$ coordinates,

$$\chi(\mathbf{x}; y_1, y_2, y_3) = F_\tau(y_2, y_3)\chi_\tau(\mathbf{x}; y_1) \quad \tau = 1, \dots, M \tag{11}$$

$\tau$ denotes summation, $F_\tau$ and $M$ were defined in Section 2.1. The Hierarchical Legendre Expansion (HLE) (Pagani, de Miguel, Petrolo, & Carrera, 2016) was chosen as $F_\tau$. The Blending Function Method (BFM) (Gordon & Hall, 1973) is used to describe the exact geometry of an arbitrary component in the $y_2 - y_3$ plane using mapping functions. The model's geometry is fixed, and the order of the analysis is chosen through the polynomial order of the structural theory. As in the previous section, an FE approximation is made, and the fluctuation unknowns are interpolated with 1D shape functions of the $y_1$ coordinate,

$$\chi_\tau(\mathbf{x}; y_1) = F_\tau(y_2, y_3) N_i(y_1)\chi_{\tau i}(\mathbf{x}) \quad i = 1, \dots, N_n \tag{12}$$

$\chi_{\tau i}(\mathbf{x})$ is the nodal unknown vector, and $N_n$ is the number of nodes in the beam element. The geometrical relations are the following:

$$\boldsymbol{\epsilon} = \bar{\boldsymbol{\varepsilon}} + \mathbf{D}\chi \tag{13}$$

$\mathbf{D}$ is a differential operator containing the geometrical relations between strains and displacements. Eq. (10) can be rewritten as follows to solve the micromechanical problem numerically:

$$\Pi = \frac{1}{2}\int_V (\bar{\boldsymbol{\varepsilon}} + \mathbf{D}\chi)^T \mathbf{C} (\bar{\boldsymbol{\varepsilon}} + \mathbf{D}\chi) dV \tag{14}$$

with periodic boundary constraints laying on the sides of the RUC cross-section, $\chi^+_\tau = \chi^-_\tau$, and for the sections orthogonal to the fibre, $\chi_{\tau 1} = \chi_{\tau n}$, in which 1 and $n$ denote the first and last beam nodes. By substituting Eq. (12) into Eq. (11), and the latter into Eq. (10), the functional $\Pi$ can be expressed in CUF form as:

$$\Pi = \frac{1}{2}\left(\chi^T_{js}\mathbf{E}^{ij\tau s}\chi_{i\tau} + 2\chi^T_{js}\mathbf{D}^{sj}_{h\varepsilon}\bar{\boldsymbol{\varepsilon}} + \bar{\boldsymbol{\varepsilon}}^T\mathbf{D}_{\varepsilon\varepsilon}\bar{\boldsymbol{\varepsilon}}\right) \tag{15}$$

$\mathbf{E}^{ij\tau s}$ and $\mathbf{D}^{sj}_{h\varepsilon}$ are the fundamental nuclei of the RUC problem, and $\mathbf{D}_{\varepsilon\varepsilon}$ is the effective stiffness matrix of the material. For the sake of brevity, the explicit expressions of the mentioned matrices are not reported in this manuscript but can be found in de Miguel et al. (2017). Apexes $\tau, s$ are related to the loop over the cross-sectional expansions, whereas $i, j$ refer to the beam nodes. Any order

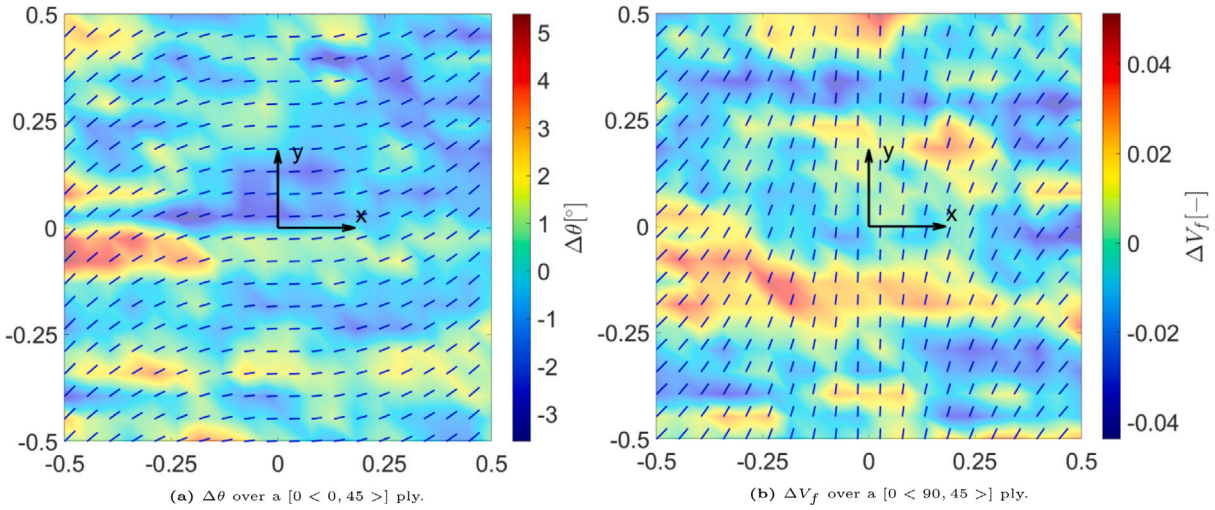


(a) $\Delta\theta$ over a $[0 < 0, 45 >]$ ply. (b) $\Delta V_f$ over a $[0 < 90, 45 >]$ ply.

**Fig. 3.** Aleatory realizations of two random fields. Fibre waviness over a $[0 < 0, 45 >]$ ply is available in (a), whereas (b) shows the variability of the fibre volume fraction over a $[0 < 90, 45 >]$ ply.

theory and beam discretization can be automatically generated by opportunely expanding the fundamental nuclei along with $\tau, s, i$ and $j$, as stated in Carrera et al. (2014).

The solution that minimizes the functional in Eq. (15) is obtained by assuming that $\chi_{\tau i} = \chi^0_{\tau i}\bar{\varepsilon}$. Therefore, the solution to the computational problem is obtained by solving the following system of equations:

$$\mathbf{E}^{ij\tau s}\chi^0_{\tau i} = -\mathbf{D}^{sj}_{h\varepsilon} \tag{16}$$

in which $\chi^0_{\tau i}$ is a $3 \times 6$ array containing the fluctuation solutions. In this regard, following the procedure depicted in de Miguel et al. (2017), the effective stiffness matrix $\mathbf{C}^*$ is calculated as:

$$\mathbf{C}^* = \frac{1}{V}\left(\chi^{0T}_{\tau i}\mathbf{D}^{sj}_{h\varepsilon} + \mathbf{D}_{\varepsilon\varepsilon}\right) \tag{17}$$

where $\mathbf{C}^*$ contains the material properties of the equivalent homogenized body.

The local stress field over the RUC can be retrieved by reintroducing the fluctuation solutions $\chi^0_{i\tau}$ into the geometrical and constitutive definitions. Hence, the local strain is computed as:

$$\boldsymbol{\varepsilon} = \bar{\boldsymbol{\varepsilon}} + \mathbf{D}(F_\tau N_i \chi^0_{i\tau}\bar{\boldsymbol{\varepsilon}}) \tag{18}$$

and the local stresses are directly calculated from Hooke's law of the original heterogeneous material

$$\boldsymbol{\sigma} = \mathbf{C}\boldsymbol{\varepsilon}. \tag{19}$$

## 3. Multiscale uncertainty modelling and through-the-scales propagation

The inclusion of the fibre volume fraction, $V_f$, and in-plane waviness, $\Delta\theta$, variability due to the steering process is modelled through Gaussian stochastic fields. In the case of laminated structures, let us denote as $H^k(x, y)$ the $k$th layer's random field. The well-known Karhunen–Loève expansion (KLE) is used to generate such a spatial distribution of the stochastic parameter (Ghanem & Spanos, 1991),

$$H^k(x, y; \omega) = \tilde{H}^k + \Delta H^k(x, y; \omega) = \tilde{H}^k + \sigma^k_H \sum_{i=1}^{\infty} \xi_i(\omega)\sqrt{\lambda_i}\varphi_i(x, y) \tag{20}$$

$\Delta H^k(x, y; \omega)$ represents the Gaussian variation of the field about its mean value $\tilde{H}^k$, $\xi_i(\omega)$ are standard Gaussian ($N \sim (0, 1)$) uncorrelated random variables, $\lambda_i$ and $\varphi_i(x, y)$ are the eigenvalues and eigenfunctions of an autocovariance integral (see Betz, Papaioannou, and Straub (2014)). $\omega$ denotes the stochastic nature of the random distributions. As stated before, the fibre volume fraction and waviness are considered herein and are represented by $H^k$. The waviness affects the nominal fibre path $\theta^k(x, y)$, and the corresponding random field is expressed as: $\Theta^k = \theta^k(x, y) + \Delta\Theta^k(x, y; \omega)$. Fig. 3 shows a realization of the two random fields accounted for in this work. The waviness is represented over a $[0 < 0, 45 >]$ lamina, and the fibre volume fraction oscillations are shown over a $[0 < 90, 45 >]$ ply.

The through-the-scales defect propagation is illustrated in Fig. 4. First, the uncorrelated random variables $\xi_i(\omega)$, defining the different KLE stochastic fields, are generated before running each analysis. Then, when calculating the stiffness matrix, at each integration point, a random value of $V_f$ provides the value of the homogenized material elastic properties used to calculate

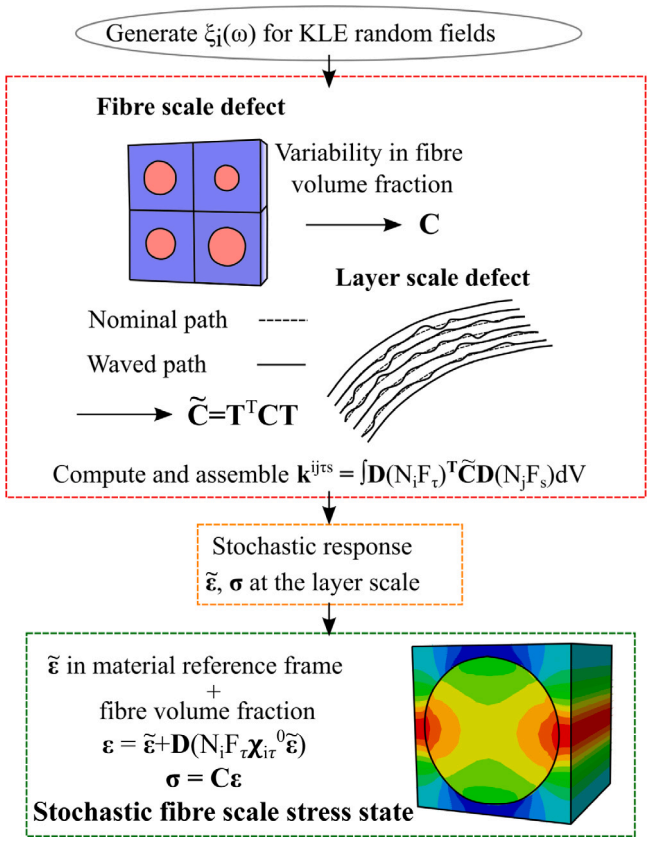


**Fig. 4.** Flow-chart of the multiscale defect propagation to retrieve stress distributions and at the different scales.

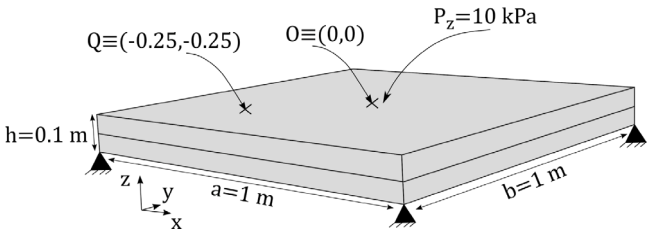


**Fig. 5.** VAT plate for numerical assessments, simply-supported on all four edges, and a uniform pressure $P_z$ on the top surface.

the material coefficient matrix **C**. The value of the elastic properties as a function of $V_f$ are obtained by micromechanical homogenization, as in Sanchez-Majano, Pagani, et al. (2021). Afterwards, the misalignment $\Delta\Theta$ is imposed when calculating the material coefficient matrix in the global reference frame ($\check{\mathbf{C}}$), which is then used for the computation of $\mathbf{k}^{ij\tau s}$. Subsequently, the structure's stiffness matrix is assembled, and the stochastic structural response is obtained. Likewise, the strain tensor of the structure in the material reference frame can be used along with the local $V_f$ to perform the dehomogenisation and retrieve the microscale stress state. As one can perceive, fibre waviness and fibre volume fraction only affect the elastic properties of the composite material. However, variability of the strength properties of the material can also be accounted for, as in Choi, Jung, Zhang, and Yun (2022), if interested in damage propagation.

## 4. Numerical results

### 4.1. Verification of the macroscale model for VAT laminates

Before conducting any microscale analysis, the layer scale model is verified. For such purpose, a simply-supported plate, whose fibre paths are denoted as $\theta = [\phi^1 < T_0^1, T_1^1 >, \phi^2 < T_0^2, T_1^2 >]$, is studied. For the analysed plate, the fibre path parameters take the

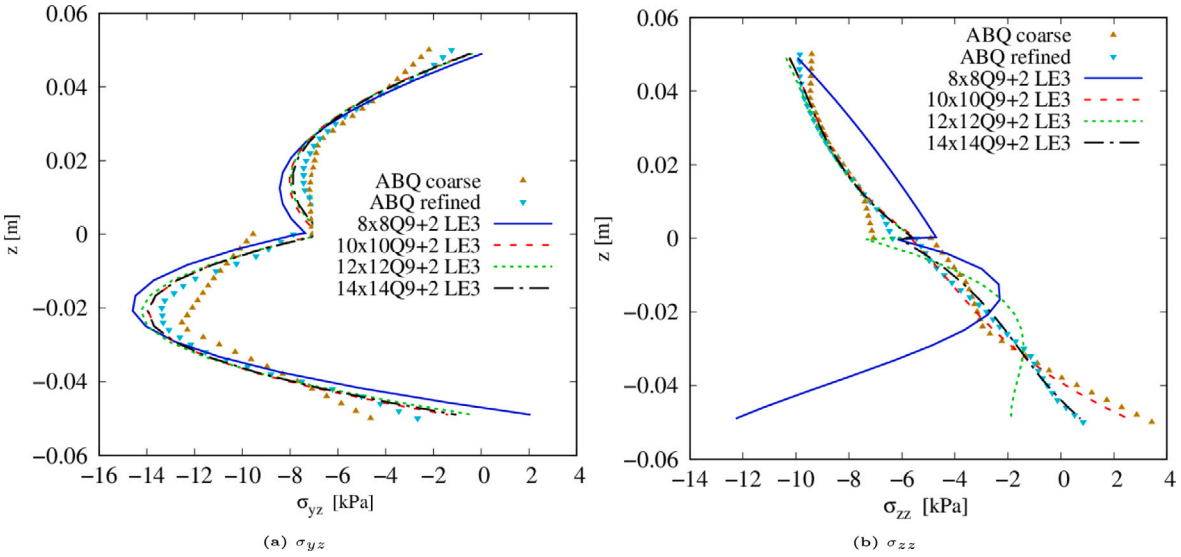


**Fig. 6.** Through-the-thickness stress field, measured at point Q, of the simply-supported $[0 < 90, 45 >, 0 < 0, 45 >]$ thick $(a/h = 10)$ laminate for the different number of mesh elements. A LW model is achieved by employing 2 LE3 elements in the thickness direction.

**Table 1**
Homogenized elastic properties of the material used for the analysis of the VAT plate. Fibre volume fraction is assumed to be $V_f = 0.60$.

| $E_1$ [GPa] | $E_2 = E_3$ [GPa] | $G_{12}$ [GPa] | $G_{23}$ [GPa] | $\nu_{12}$ [-] | $\nu_{23}$ [-] |
|---|---|---|---|---|---|
| 143.17 | 9.64 | 6.09 | 3.12 | 0.252 | 0.349 |

**Table 2**
Vertical displacement of the simply-supported $[0 < 90, 45 >, 0 < 0, 45 >]$ thick $(a/h = 10)$ plate evaluated at point Q for different FE meshes. Each discretization employs 2 LE3 elements through the thickness direction.

| Model | DOF | $-u_z \cdot 10^5$ [m] |
|---|---|---|
| ABQ coarse | 45387 | 1.59 |
| ABQ refined | 334611 | 1.60 |
| 8 × 8 Q9 | 6069 | 1.43 |
| 10 × 10 Q9 | 9261 | 1.45 |
| 12 × 12 Q9 | 13125 | 1.47 |
| 14 × 14 Q9 | 17661 | 1.47 |

**Table 3**
Stress state of the simply-supported $[0 < 90, 45 >, 0 < 0, 45 >]$ thick $(a/h = 10)$ plate evaluated at point Q and $z = -0.02$ m for different FE meshes. Each discretization employs 2 LE3 elements through the thickness direction.

| Model | DOF | $\sigma_{xx}$ [kPa] | $\sigma_{yy}$ [kPa] | $\sigma_{zz}$ [kPa] | $\sigma_{xz}$ [kPa] | $\sigma_{yz}$ [kPa] | $\sigma_{xy}$ [kPa] |
|---|---|---|---|---|---|---|---|
| ABQ coarse | 45387 | 48.56 | 12.67 | −3.15 | −6.17 | −12.08 | −20.10 |
| ABQ refined | 334611 | 48.13 | 12.38 | −2.80 | −6.27 | −13.37 | −19.12 |
| 8 × 8 Q9 | 6069 | 44.85 | 23.48 | −2.76 | −6.02 | −14.59 | −20.51 |
| 10 × 10 Q9 | 9261 | 48.28 | 22.39 | −3.10 | −7.30 | −13.93 | −20.89 |
| 12 × 12 Q9 | 13125 | 48.23 | 21.91 | −1.73 | −6.03 | −14.23 | −22.03 |
| 14 × 14 Q9 | 17661 | 48.65 | 22.88 | −2.56 | −6.95 | −13.96 | −20.47 |

following values: $\phi^1 = \phi^2 = 0°$, $T_1^1 = T_1^2 = 45°$, $T_0^1 = 90°$, and $T_0^2 = 0°$. The elastic properties of the material, considering a $V_f = 0.60$, are reported in Table 1. The plate is illustrated in Fig. 5, where the geometrical dimensions and loading condition are depicted.

First, a convergence analysis on the number of finite elements is carried out. Results are compared with the outcomes obtained with commercial software Abaqus (ABQ) (Smith, 2009). A coarse ($40 \times 40 \times 8$) and a refined ($80 \times 80 \times 16$) model comprising solid C3D8R elements were used since an evaluation of both in-plane and out-of-plane stress components is pursued. Note that the latter are not available if S4R shell-like elements are utilized. Fig. 6 illustrates the transverse shear and normal stresses for a different number of Q9 elements, ranging from 64 up to 196 FE. Each analysis utilizes 2 LE3 for the through-the-thickness discretization, hence obtaining an LW approach. Table 2 shows the vertical displacement at point Q and $z = -0.02$ m for the different FE meshes. Likewise, Table 3 presents the six stress components evaluated at the same point and FE meshes. Convergence of $u_z$ suggests that

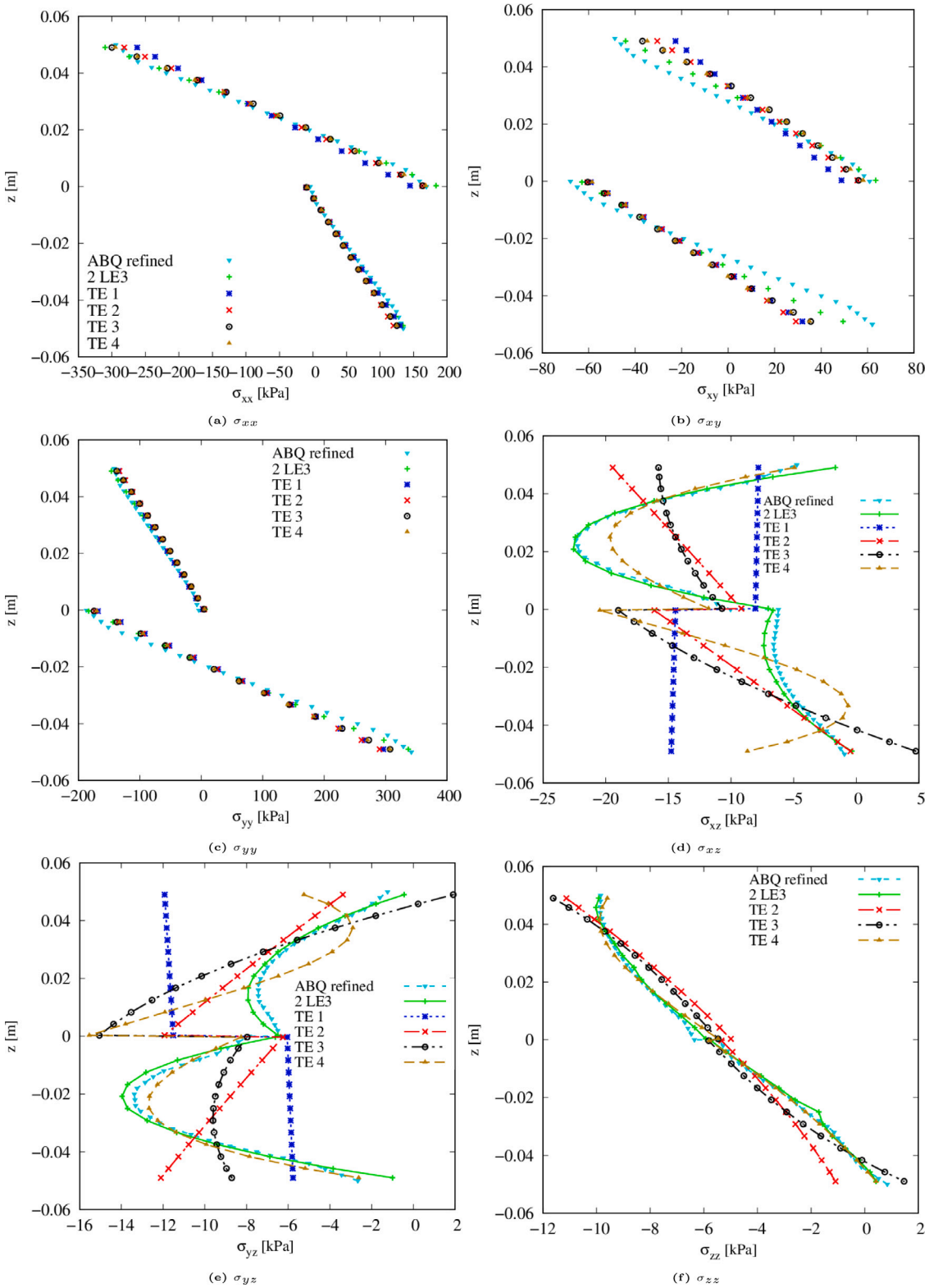


**Fig. 7.** Through-the-thickness stress field, measured at point Q, of the simply-supported $[0 < 90, 45 >, 0 < 0, 45 >]$ thick ($a/h = 10$) laminate for the different expansion functions. The employed mesh comprises 14 × 14Q9 elements. Legend in (a) applies for(b).

**Table 4**
Stress state of the simply-supported $[0 < 90, 45 >, 0 < 0, 45 >]$ thick $(a/h = 10)$ laminate at point Q and $z = -0.02$ m for different structural theories and a 14 × 14 Q9 FE mesh approximation.

| Theory | DOF | $\sigma_{xx}$ [kPa] | $\sigma_{yy}$ [kPa] | $\sigma_{zz}$ [kPa] | $\sigma_{xz}$ [kPa] | $\sigma_{yz}$ [kPa] | $\sigma_{xy}$ [kPa] |
|---|---|---|---|---|---|---|---|
| TE 1 | 5046 | 48.61 | 27.38 | 14.86 | −14.57 | −5.93 | −20.79 |
| TE 2 | 7569 | 46.27 | 25.83 | −3.32 | −9.52 | −8.78 | −20.91 |
| TE 3 | 10092 | 44.89 | 20.75 | −3.49 | −11.13 | −9.49 | −22.81 |
| TE 4 | 12615 | 45.30 | 21.73 | −2.76 | −4.75 | −12.65 | −22.65 |
| 2 LE3 | 17661 | 48.65 | 22.88 | −2.56 | −6.95 | −13.96 | −20.47 |

**Table 5**
Strain state computed in the material reference frame at point Q and $z = -0.02$ m of the simply-supported $[0 < 90, 45 >, 0 < 0, 45 >]$ thick $(a/h = 10)$ laminate. Strains are obtained with the 14 × 14 Q9 FE mesh and 2 LE3 expansion theory.

| $\varepsilon_{11}$ $[\mu\varepsilon]$ | $\varepsilon_{22}$ $[\mu\varepsilon]$ | $\varepsilon_{33}$ $[\mu\varepsilon]$ | $\varepsilon_{13}$ | $\varepsilon_{23}$ $[\mu\varepsilon]$ | $\varepsilon_{12}$ $[\mu\varepsilon]$ |
|---|---|---|---|---|---|
| −1.492 | 0.062 | −0.022 | −0.049 | −0.178 | −0.881 |

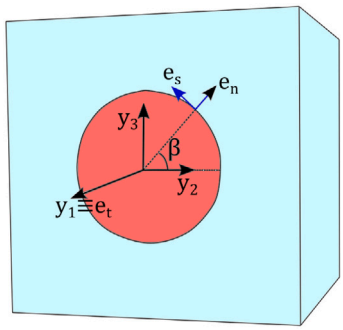


**Fig. 8.** Micromechanical cartesian and cylindrical reference frames used for the rotation of the microscale stress tensor. Axis in the fibre direction $y_1$ is coincident with tangent axis $e_t$. $\beta$ is defined as the angle between $y_2$ and the radial direction $e_n$.

14 × 14 mesh is sufficient to conduct numerical analyses. Conversely, some oscillations are appreciated in Table 3. Nevertheless, since the displacements are the primary variables, and strains and stresses are a mere postprocessing operation, the convergence of the numerical model is assured.

The ABQ models cannot capture the continuity of the out-of-plane stresses at the layers interface nor the stress free condition of the transverse shear component, as opposed to the LW CUF models. Moreover, it is observed that the ABQ coarse cannot provide the characteristic parabolic shape of $\sigma_{yz}$. These two reasons show the necessity of using a large number of solid elements to retrieve an accurate evaluation of transverse stresses.

A study concerning the chosen expansion function is carried out. Specifically, the employed cubic (LE3) LW model is compared with first- up to fourth-order TE. Table 4 provides the values predicted by the different models at point Q and $z = -0.02$ m. The stress distributions are available in Fig. 7. and show that ESL models are accurate for predicting the in-plane stress distribution. However, important discrepancies are found for the transverse components. Indeed, TE 1 cannot catch any of the out-of-plane stresses, whereas TE 4 is the only one providing relatively close results to those by the 2 LE3 model (see Figs. 7(d) and 7(e)). For that reason, LW models are used to calculate the stress distributions in the upcoming analyses.

### *4.2. Stochastic microscale analysis of thick VAT laminates*

To demonstrate the capabilities of the proposed multiscale approach, one can retrieve the local stress distribution. The followed procedure is similar to that depicted in Fig. 4 with the exception that no stochastic field is generated beforehand nor incorporated in the numerical model. The local strain field imposed to the RUC model is enlisted in Table 5. As shown in the works by de Miguel et al. (de Miguel et al., 2017), the stress distribution at the RUC level may present high gradients between the different constituents. Therefore, it is necessary to employ high-order expansions when calculating the microscale stresses. In the upcoming results, eighth-order HLE are utilized for such purpose.

The microscale stress sensitivity is performed with a total of $10^3$ Monte Carlo analyses. Such analyses comprise both the layer scale and microstructural calculations, being the former solved in the first instance. Subsequently, micro stresses are transformed into a cylindrical reference frame according to Lekhnitskii (1968), see Fig. 8, and first- and second-order statistical moments are calculated at the proximity of the fibre-matrix interface. The polar plots provide the magnitude of the stresses in the radial direction of the plot, whilst the circumferential direction represents angle $\beta$ from Fig. 8. Normal ($t_n$) and shear ($t_s$, $t_t$) stresses are represented in a polar plot in Fig. 9. The following is appreciated:

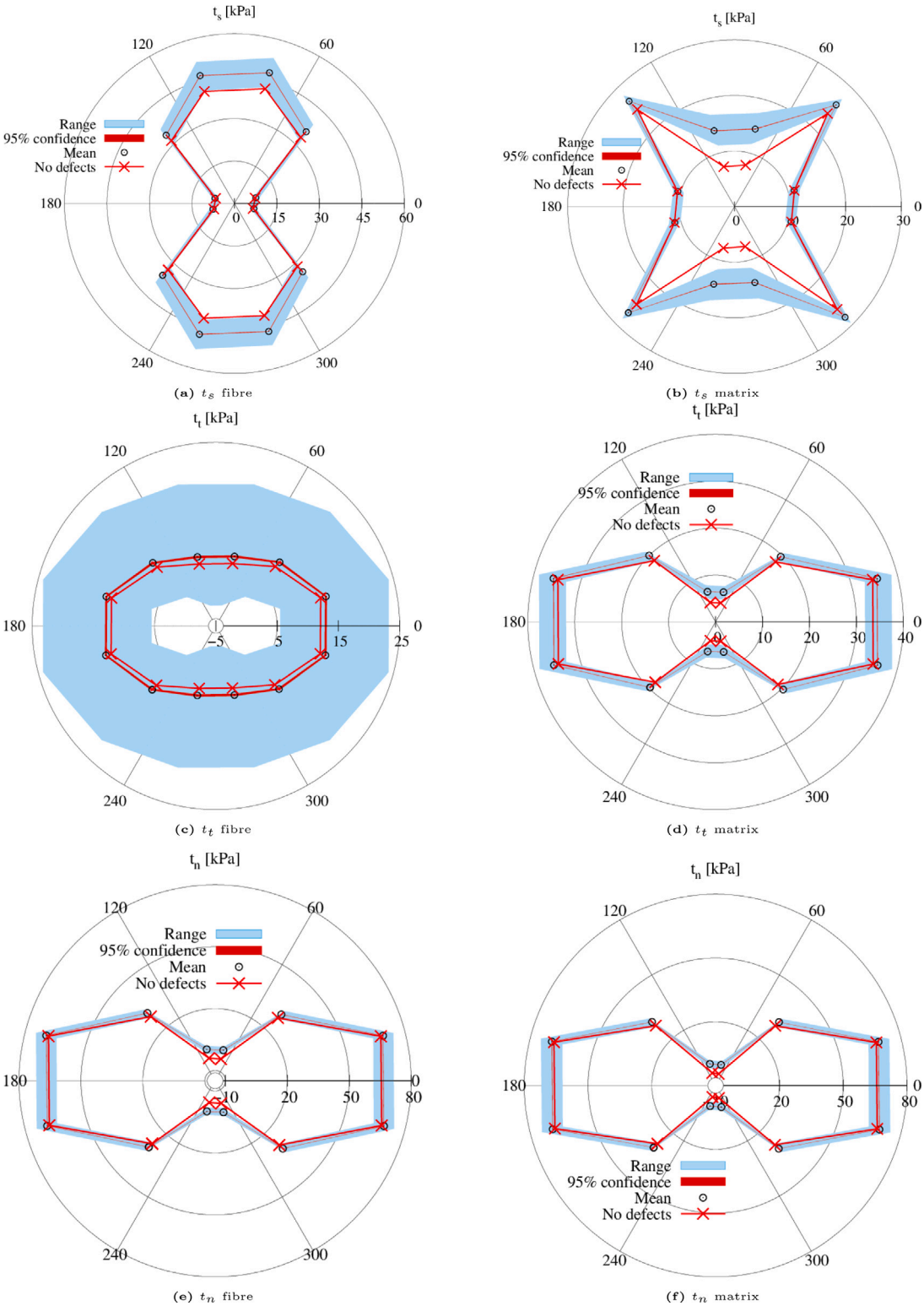


**Fig. 9.** Stress distribution of the fibre and matrix constituents at its interface, along with statistical data. Stresses are reported in a cylindrical reference frame. Data corresponds to the simply-supported $[0 < 90, 45 >, 0 < 0, 45 >]$ thick $(a/h = 10)$ laminate.

**Table 6**
Normal and shear stresses statistics of the RUC constituents at $\beta = 75°$ for the simply-supported $[0 < 90,45 >,0 < 0,45 >]$ thick ($a/h = 10$) laminate. Range indicates the minimum and maximum values registered in the Monte Carlo simulations.

| Constituent | Magnitude | $t_n$ [kPa] | $t_s$ [kPa] | $t_t$ [kPa] |
|---|---|---|---|---|
| Fibre | No defects | −4.08 | 41.96 | 5.55 |
| | Mean | 0.31 | 47.82 | 6.74 |
| | 95% interval | [0.27,0.35] | [47.72,47.93] | [6.54,6.94] |
| | Range | [−1.61,2.02] | [42.60,53.20] | [−1.52,18.93] |
| Matrix | No defects | −4.36 | 7.73 | 4.18 |
| | Mean | 0.03 | 14.43 | 6.53 |
| | 95% interval | [0,0.07] | [14.37,14.50] | [6.51,6.57] |
| | Range | [−2.04,1.76] | [11.67,17.42] | [4.95,7.88] |

**Table 7**
Vertical displacement of the simply-supported $[0 < 90,45 >,0 < 0,45 >]$ thin ($a/h = 100$) laminate evaluated at point O for different FE meshes. Each discretization employs 2 LE3 elements through the thickness direction.

| Model | DOF | $-u_z \cdot 10^3$ [m] |
|---|---|---|
| 8 × 8 Q16 | 13125 | 7.14 |
| 10 × 10 Q16 | 20181 | 7.18 |
| 12 × 12 Q16 | 28799 | 7.22 |
| 14 × 14 Q16 | 38829 | 7.25 |
| 16 × 16 Q16 | 50421 | 7.27 |
| 20 × 20 Q16 | 76141 | 7.31 |

**Table 8**
Stress state of the simply-supported $[0 < 90,45 >,0 < 0,45 >]$ thin ($a/h = 100$) laminate evaluated at point Q and $z = -2$ mm for different FE meshes. Each discretization employs 2 LE3 elements through the thickness direction.

| Model | DOF | $\sigma_{xx}$ [MPa] | $\sigma_{yy}$ [MPa] | $\sigma_{zz}$ [kPa] | $\sigma_{xz}$ [kPa] | $\sigma_{yz}$ [kPa] | $\sigma_{xy}$ [MPa] |
|---|---|---|---|---|---|---|---|
| 8 × 8 Q16 | 13125 | −0.538 | −2.69 | 86.98 | −59.05 | −42.22 | −1.50 |
| 10 × 10 Q16 | 20181 | −0.668 | −2.82 | −15.04 | −124.35 | −116.56 | −1.54 |
| 12 × 12 Q16 | 28799 | −0.614 | −2.78 | −15.86 | −96.88 | −98.85 | −1.53 |
| 14 × 14 Q16 | 38829 | −0.642 | −2.85 | 1.62 | −120.19 | −111.15 | −1.57 |
| 16 × 16 Q16 | 50421 | −0.621 | −2.85 | 3.99 | −109.37 | −104.76 | −1.57 |
| 20 × 20 Q16 | 76141 | −0.624 | −2.89 | −0.007 | −114.69 | −107.23 | −1.60 |

- Circumferential stresses, see Figs. 9(a) and 9(b), are the ones showing the largest differences between the nominal stresses and the mean value, especially in the range $\beta = 45$–$135°$ and $\beta = 225$–$315°$. Note that in the mentioned ranges the flawless stresses are below the maximum–minimum range of the stochastic analysis, see Table 6.
- The fibre's longitudinal stress ($t_t$) distribution in Fig. 9(c) presents an oval shape whose maximum is below 15 kPa and its minimum about 7 kPa. Conversely, the matrix shows a two-lobed shape with peak values about 35 kPa in $\beta = 0°$ and $\beta = 180°$ in Fig. 9(d).
- Radial stresses ($t_n$) in Figs. 9(e) and 9(f) present almost no differences between fibre and matrix constituents. That is correct since continuity of radial stresses has to be guaranteed in the normal direction to the fibre-matrix interface.
- Very small variability is appreciated overall. The 95% confidence intervals are very shallow and the maximum–minimum ranges do not provide a large variations, with the exception of fibre's $t_t$.

### 4.3. Macroscale and stochastic microscale analysis of thin VAT laminates

A similar analysis is now conducted for the case of thin VAT laminates. In this case, the previous plate, with the same boundary and loading conditions, material and fibre path orientations is considered. The only difference between both structures is that the present one comprises a length-to-thickness ratio equal to $a/h = 100$, whereas in the precedent study that ratio equalled $a/h = 10$. A convergence analysis was conducted using bi-quadratic Q9 elements for the in-plane mesh and cubic elements for the through-the-thickness discretization. Besides, the authors employed the Mixed Interpolation of Tensorial Components (MITC) (Carrera, Cinefra, & Nali, 2010) strategy over Q9 elements to avoid shear locking phenomena that arises in thin plates. Both Q9 and MITC Q9 strategies did not successfully compute the out-of-plane stress components. They are not reported in the manuscript for the sake of conciseness and brevity. Hence, bi-cubic Q16 elements were implemented to conduct the convergence study. The vertical displacements, computed at $O \equiv (0,0)$, are enlisted in Table 7. Likewise, stresses calculated at point Q and $z = -2$ mm are enlisted in Table 8. Although the same value of the primary variables is not achieved for the finest meshes (16 × 16 Q16 and 20 × 20 Q16), a convergence is appreciated as the mesh refinement progresses. A similar thing occurs for the stress components, especially in-plane terms, as appreciated in Table 8. This fact is more evident by observing Fig. 10. Albeit not completely identical, a 0.8% relative difference in $u_z$ between the 14 × 14 Q16 and 20 × 20 Q16 is calculated, presenting the former twofold reduction in terms of DOF

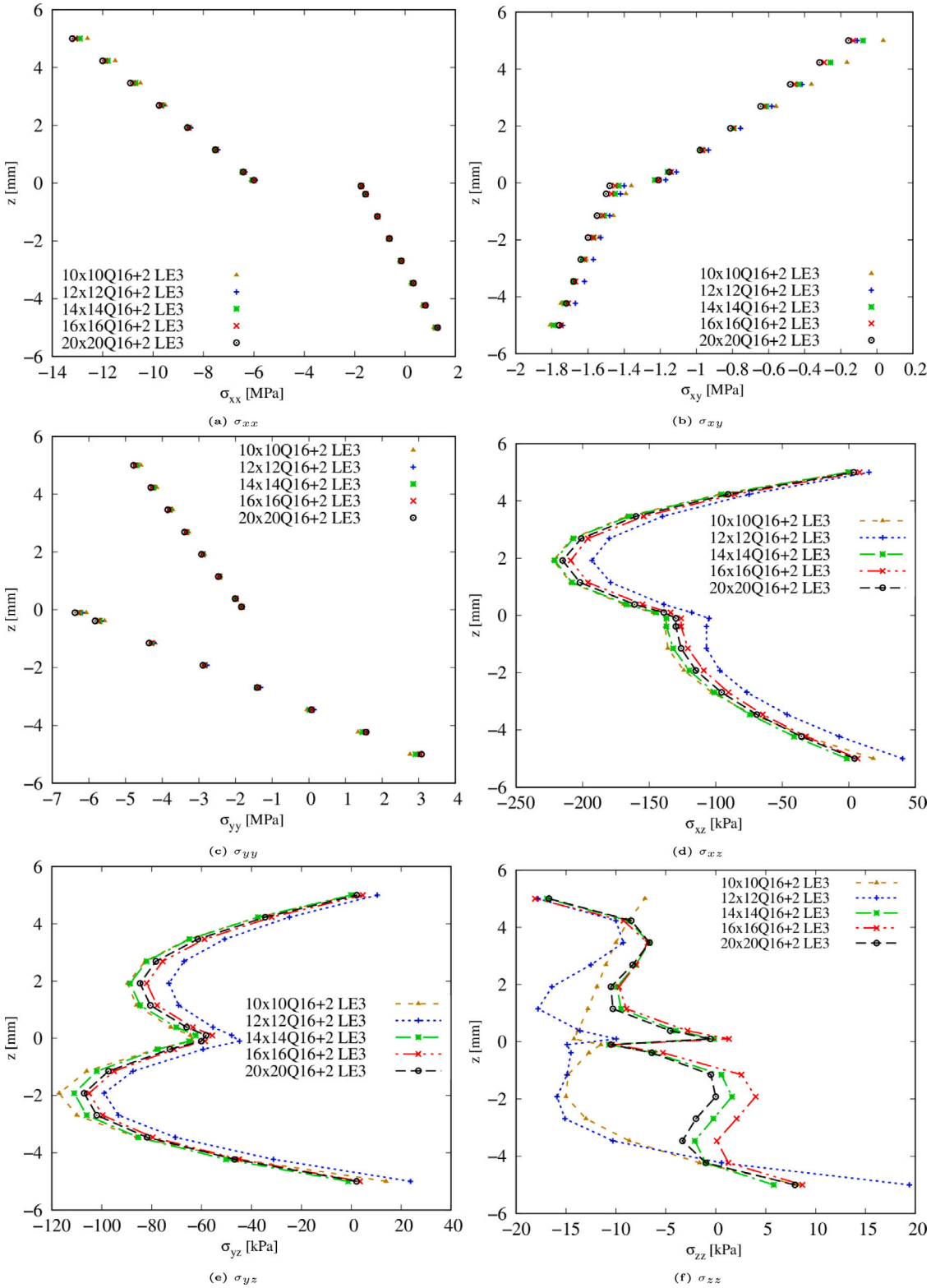


**Fig. 10.** Through-the-thickness stress field, measured at point Q, of the simply-supported $[0 < 90, 45 >, 0 < 0, 45 >]$ thin $(a/h = 100)$ laminate for the different number of mesh elements. A LW model is achieved by employing 2 LE3 elements in the thickness direction.

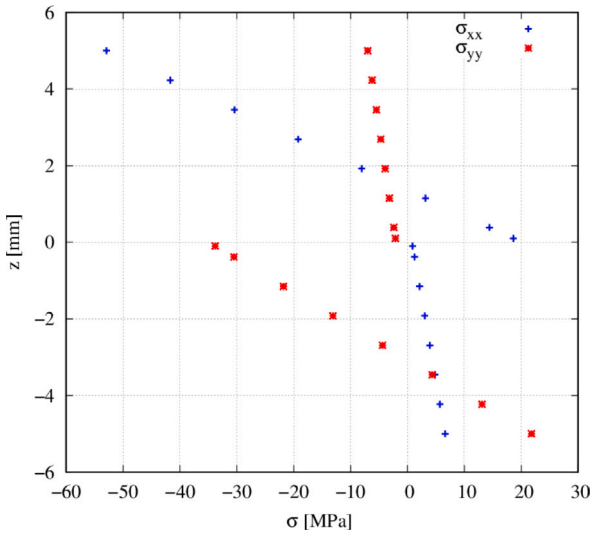


**Fig. 11.** Through-the-thickness normal in-plane stresses, measured at point O, of the simply-supported $[0 < 90, 45 >, 0 < 0, 45 >]$ thin $(a/h = 100)$ laminate. The employed mesh comprises 14 × 14Q16 elements and 2 LE3 through the thickness direction.

**Table 9**
Strain state computed in the material reference frame at points presenting the minimum and maximum values of $\sigma_{xx}$ and $\sigma_{yy}$, respectively. Strains are obtained with the 14 × 14 Q16 FE mesh and 2 LE3 expansion theory.

| Case | $\varepsilon_{11}$ $[\mu\varepsilon]$ | $\varepsilon_{22}$ $[\mu\varepsilon]$ | $\varepsilon_{33}$ $[\mu\varepsilon]$ | $\varepsilon_{13}$ | $\varepsilon_{23}$ $[\mu\varepsilon]$ | $\varepsilon_{12}$ $[\mu\varepsilon]$ |
|---|---|---|---|---|---|---|
| Minimum $\sigma_{xx}$ | −631.29 | −357.37 | 343.82 | −1.40 | 3.89 | 166.47 |
| Maximum $\sigma_{yy}$ | 646.99 | 140.63 | −276.38 | 2.96 | 1.36 | −342.436 |

and computation time, which is essential when performing a multiscale sensitivity analysis. For that reason, the 14 × 14 Q16 mesh is employed in the upcoming results.

Once a convergent numerical model is obtained, $10^3$ Monte Carlo simulations are performed following the procedure depicted in Fig. 4. In the case of thin plates it is more interesting to pay attention to the maximum, in absolute value, in-plane stresses that occur at the layer scale for the nominal structure. They are located at point O of the structure. The maximum compression and tension stresses are $\sigma_{xx}$ at $z = 5$ mm and $\sigma_{yy}$ at $z = -5$ mm, as appreciated in Fig. 11. Therefore, a study of the stresses at the fibre scale is conducted next at these points. The deformations computed in the material reference frame of these two points are enlisted in Table 9.

The case showing the maximum compressive stress is analysed first. The microscale stress state is represented in Fig. 12. The following comments are made:

- Circumferential components $t_s$ are shown in Figs. 12(a) and 12(b). The former presents an oval shape, ranging from −5 MPa to −2 MPa in the nominal case. The latter shows a four-lobed distribution in which stresses vary between −3 MPa and −0.5 MPa, and presenting the highest compression values at $\beta = 45, 135, 225, 315°$.
- The longitudinal stresses are represented in Figs. 12(c) and 12(d). A constant value is found for the fibre of about −85 MPa, whilst a tow-lobed shape is present for the matrix, with peak compression values at $\beta = 0°$ and $\beta = 180°$.
- Figs. 12(e) and 12(f), and Table 10 demonstrate the continuity of the normal stress component, which presents a peak value of about 0.50 MPa at $\beta = 90°$ and $\beta = 270°$.
- A small variability is appreciated when comparing the pristine distribution with its stochastic counterparts, with the exception of Figs. 12(a) and 12(b) in the ranges $\beta = 75$–$135°$ and $\beta = 255$–$295°$, where differences of even 1 MPa arise. The fibre's longitudinal stress is the one undergoing a larger variability in terms of maximum–minimum range, as occurred in the previous case.

The case presenting the maximum tensile stress is depicted hereinafter. It corresponds to the maximum value of $\sigma_{yy}$, which is located in point O and $z = -5$ mm. The microscale stress state is represented in Fig. 13. The next statements are said:

- Figs. 13(a) and 13(b) show the circumferential stress $t_s$. The former presents a two-lobed shape where the peak values are located at $\beta = 90°$ and $\beta = 270°$, whereas the latter presents its peak values at $\beta = 45, 135, 225, 315°$.
- Longitudinal stresses are available in Figs. 13(c) and 13(d). The fibre undergoes constant tension stress of 35 MPa, whilst the matrix presents a two-lobed shape with peak values of about 3.5 MPa appearing when $\beta = 0°$ and $\beta = 180°$.
- The radial stress continuity is demonstrated in Figs. 13(e) and 13(f), and Table 11, where slight differences are appreciated. The radial stresses would contribute to the failure onset due to its tensile character.

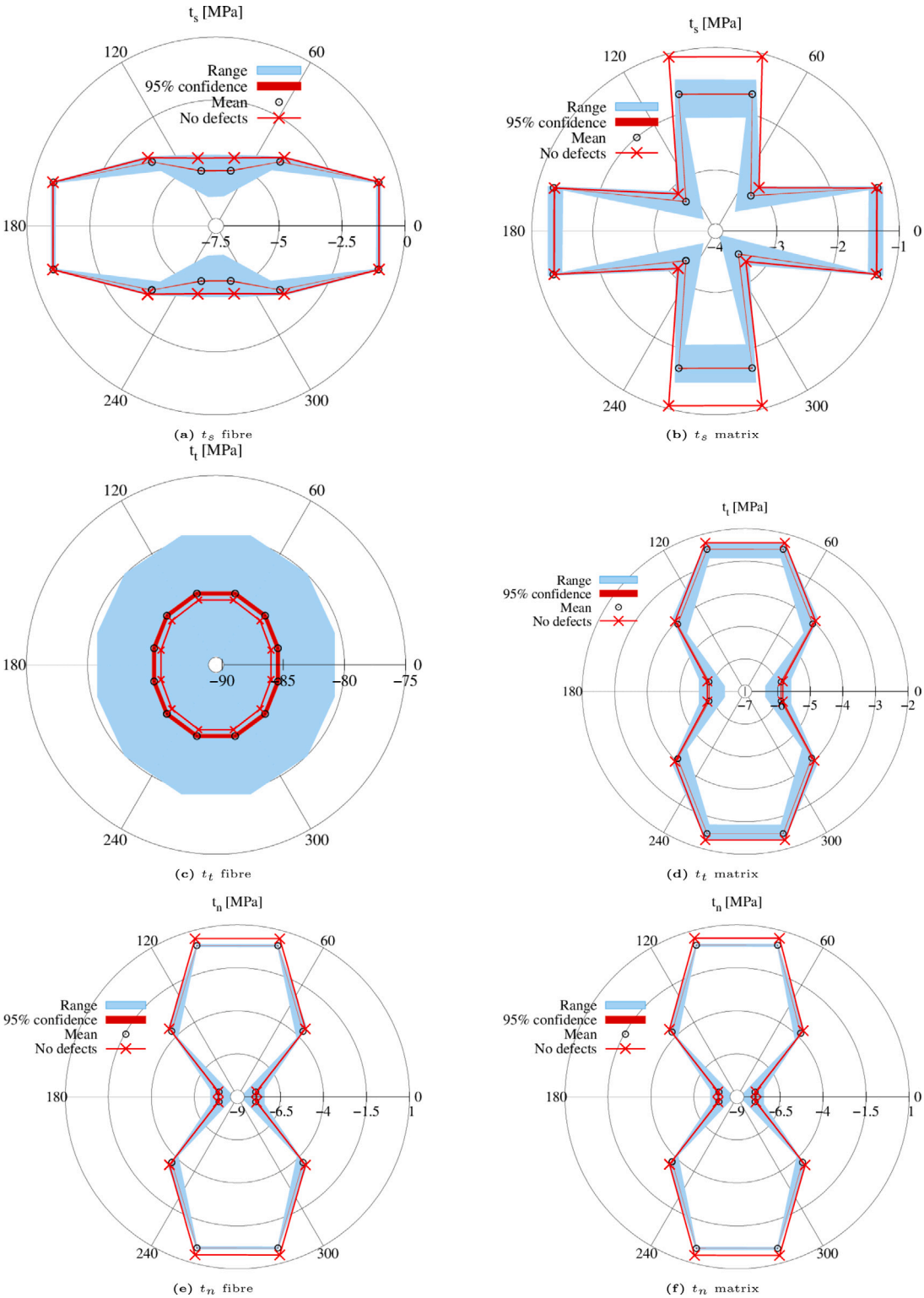


**Fig. 12.** Stress distribution of the fibre and matrix constituents at its interface, along with statistical data. Stresses are reported in a cylindrical reference frame. Data corresponds to the simply-supported $[0 < 90, 45 >, 0 < 0, 45 >]$ thin $(a/h = 100)$ laminate and minimum $\sigma_{xx}$.

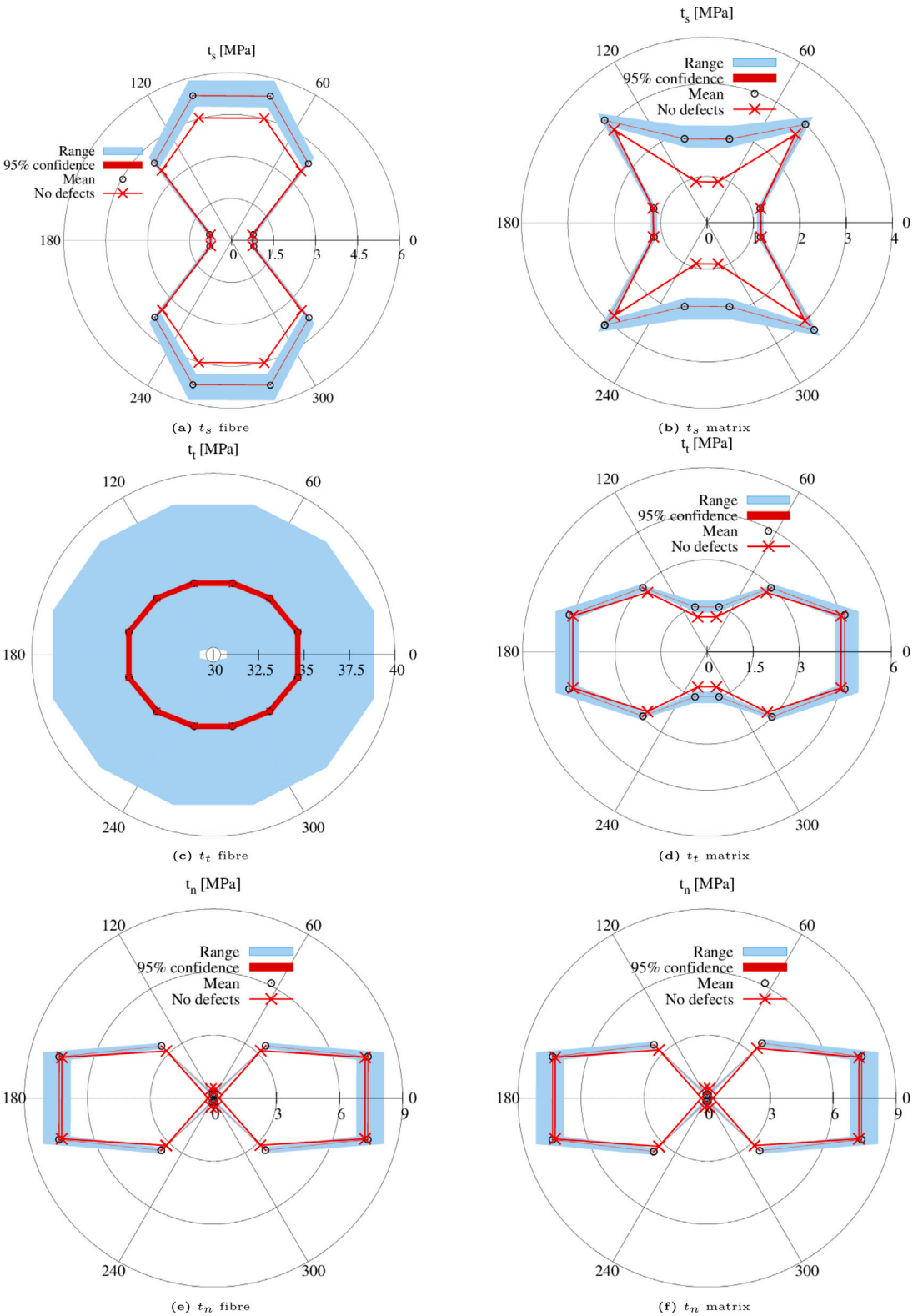


**Fig. 13.** Stress distribution of the fibre and matrix constituents at its interface, along with statistical data. Stresses are reported in a cylindrical reference frame. Data corresponds to the simply-supported $[0 < 90, 45 >, 0 < 0, 45 >]$ thin $(a/h = 100)$ laminate and maximum $\sigma_{yy}$.

**Table 10**
Normal and shear stresses statistics of the RUC constituents at $\beta = 75°$ for the thin laminate's minimum value of $\sigma_{xx}$. Range indicates the minimum and maximum values registered in the Monte Carlo simulations.

| Constituent | Magnitude | $t_n$ [MPa] | $t_s$ [MPa] | $t_t$ [MPa] |
|---|---|---|---|---|
| Fibre | No defects | 0.52 | −4.71 | −85.01 |
| | Mean | 0.091 | −5.23 | −84.46 |
| | 95% interval | [0.087,0.094] | [−5.26,−5.21] | [−84.64,−84.28] |
| | Range | [0,0.18] | [−6.28,−4.58] | [−89.78,−79.54] |
| Matrix | No defects | 0.54 | −1.05 | −2.27 |
| | Mean | 0.12 | −1.68 | −2.48 |
| | 95% interval | [0.11,0.12] | [−1.69,−1.67] | [−2.49,−2.47] |
| | Range | [0.02,0.21] | [−2.08,−1.44] | [−2.77,−2.27] |

**Table 11**
Normal and shear stresses statistics of the RUC constituents at $\beta = 75°$ for the thin laminate's minimum value of $\sigma_{yy}$. Range indicates the minimum and maximum values registered in the Monte Carlo simulations.

| Constituent | Magnitude | $t_n$ [MPa] | $t_s$ [MPa] | $t_t$ [MPa] |
|---|---|---|---|---|
| Fibre | No defects | −0.44 | 4.52 | 34.03 |
| | Mean | 0.194 | 5.34 | 34.07 |
| | 95% interval | [0.191,0.197] | [5.32,5.35] | [33.91,34.24] |
| | Range | [0.05,0.31] | [4.93,5.91] | [30.07,38.56] |
| Matrix | No defects | −0.47 | 0.91 | 1.17 |
| | Mean | 0.166 | 1.87 | 1.51 |
| | 95% interval | [0.163,0.169] | [1.86,1.88] | [1.50,1.52] |
| | Range | [−0.007,0.286] | [1.67,2.16] | [1.32,1.73] |

- A small variability of the stresses in terms of nominal, mean and 95% confidence interval is observed, with just two exceptions. They are evidenced in Figs. 13(a) and 13(b) in the ranges $\beta = 45$–$135°$ and $\beta = 225$–$315°$, where maximum discrepancies of 0.5 MPa and 1 MPa can be appreciated. Finally, the fibre's longitudinal stress $t_t$ is the one presenting the largest maximum–minimum range.
- A similar distribution to the one presented for the thick plate is observed since, in both cases, layer scale $\sigma_{xx}$ and $\sigma_{yy}$ have a tension character. Nevertheless, some differences are appreciated. First, the shape of $t_t$ distribution has an oval shape in Fig. 9(c), whereas a circular one is available in Fig. 13(c).
- Concerning $t_t$, in the case of the thin laminate there exists a one-order-of-magnitude difference between the one that the fibre undergoes, Fig. 13(c), and that of the matrix, Fig. 13(d). On the contrary, such difference in order of magnitude is not appreciated in the case of the thick plate, as evidenced in Figs. 9(c) and 9(d).
- Regarding $t_n$, a highest stress gradient is appreciated in the proximities of $\beta = 90°$ and $\beta = 270°$ in the case of the thin plate, see Fig. 13(e), when compared to the thick plate, Fig. 9(e).

## 5. Conclusions

This work has presented an effective approach for the multiscale linear static analysis of VAT composite plates based on 2D and 1D refined CUF FE for the mesoscale and microscale, respectively. Additionally, fibre scale and layer scale uncertainty defects were featured in the modelling without additional computational cost by means of KLE-generated random fields.

The necessity of an accurate prediction of the stresses at the layer scale has been demonstrated for both thick ($a/h = 10$) and thin ($a/h = 100$) VAT laminates. For such purpose, LW models have been proven to perform better against ESL models, especially if transverse components are of interest. The ESL models employed in this work could not capture the transverse shear stress distribution for the thick layer. In this regard, they would have difficulties to predict the same distributions when thin laminates are involved because of the shear locking phenomena. Chasing an adequate out-of-plane stress retrieval implied an increase in the polynomial order of the shape functions employed in the thin laminate, moving from bi-quadratic (Q9) to bi-cubic (Q16) elements, while maintaining cubic elements for the through-the-thickness discretization. In this manner, the 3D stress state of the composite material can be accurately characterized from the fibre-matrix scale up to the layer scale.

The layer scale strains of both VAT structures were computed in the material reference system and used as input for the computation of the fibre scale stresses in a cylindrical reference system by means of 1D CUF-MSG models. Results showed a significant difference between the nominal microscale circumferential stresses $t_s$ and the mean value of its stochastic counterparts. In the case where layer scale stresses had a tensile character, the maximum differences appear in the proximities of $\beta = 90°$ and $\beta = 270°$ for both fibre and matrix, see Figs. 9(a) and 13(a), and Figs. 9(b) and 13(b). Conversely, those differences were only present in the matrix's $t_s$ when $\beta$ is close to 90° and 270°. For either tension and compression character, it was the fibre longitudinal stress $t_t$ the one showing a larger variability in terms of maximum–minimum range. Additionally, the continuity of the normal stress $t_n$ between fibre and matrix was guaranteed by using high-order expansion functions that provide a geometrically exact shape of the micromechanical model. The stress continuity is of utmost importance since $t_n$ participates in the commonly used mixed-mode

criteria when analysing micromechanics damage initiation. A higher stress gradient was appreciated in Fig. 13(e) for the thin plate's $t_n$ around $\beta = 90°$ and $\beta = 270°$ when compared to the same magnitude of the thick plate (see Fig. 9(e)). Such high gradient could be deleterious in terms of damage propagation in the case that further loading might be applied, due to the tensile character of $t_n$. However, this work was strictly related to the failure onset of VAT composites, thus remaining in the linear elastic behaviour of the material. Some studies have already analysed the progressive failure and delamination of composites employing high-order CUF beam elements, see Kaleel et al. (2020, 2018).

## Declaration of competing interest

The authors declare the following financial interests/personal relationships which may be considered as potential competing interests:Alfonso Pagani reports financial support was provided by European Research Council.

## Data availability

Data will be made available on request.

## Acknowledgements

This work is part of a project that has received funding from the European Research Council (ERC) under the European Union's Horizon 2020 research and innovation programme (Grant agreement No. 850437).

## References

Aboudi, J. (1989). Micromechanical analysis of composites by the method of cells. *Applied Mechanics Review*, *42*(7), 193–221.
Akbarzadeh, A. H., Arian Nik, M., & Pasini, D. (2014). The role of shear deformation in laminated plates with curvilinear fiber paths and embedded defects. *Composite Structures*, *118*, 217–227.
Balokas, G., Kriegesmann, B., Czichon, S., & Rolfes, R. (2019). Stochastic modeling techniques for textile yarn distortion and waviness with 1D random fields. *Composites Part A: Applied Science and Manufacturing*, *127*, Article 105639.
Betz, W., Papaioannou, I., & Straub, D. (2014). Numerical methods for the discretization of random fields by means of the Karhunen–Loève expansion. *Computer Methods in Applied Mechanics and Engineering*, *271*, 109–129.
Carrera, E. (2002). Theories and finite elements for multilayered, anisotropic, composite plates and shells. *Archives of Computational Methods in Engineering*, *9*(2), 87–140.
Carrera, E. (2003). Theories and finite elements for multilayered plates and shells: A unified compact formulation with numerical assessment and benchmarking. *Archives of Computational Methods in Engineering*, *10*(3), 215–296.
Carrera, E., Cinefra, M., & Nali, P. (2010). MITC technique extended to variable kinematic multilayered plate elements. *Composite Structures*, *92*(8), 1888–1895.
Carrera, E., Cinefra, M., Petrolo, M., & Zappino, E. (2014). *Finite element analysis of structures through unified formulation*. Hoboken, New Jersey, USA: Wiley & Sons.
Cauchy, A. L. (1828). Sur l'equilibre et le mouvement d'une plaque solide. *Exercises de Mathematique*, *3*, 328–355.
Choi, H., Jung, S., Zhang, C., & Yun, G. J. (2022). A three-dimensional stochastic progressive damage simulation model for polymer matrix-based laminate composites. *Mechanics of Advanced Materials and Structures*, *29*(5), 633–650.
Dang, H., Zhao, Z., Liu, P., Zhang, C., Tong, L., & Li, Y. (2020). A new analytical method for progressive failure analysis of two-dimensional triaxially braided composites. *Composites Science and Technology*, *186*, Article 107936.
de Miguel, A. G., Pagani, A., Yu, W., & Carrera, E. (2017). Micromechanics of periodically heterogeneous materials using higher-order beam theories and the mechanics of structure genome. *Composite Structures*, *180*, 484–496.
DiNardo, M. T., & Lagace, P. A. (1989). Buckling and postbuckling of laminated composite plates with ply dropoffs. *American Institute of Aeronautics and Astronautics*, *27*(10), 1392–1398.
Falcó, O., Lopes, C. S., Naya, F., Sket, F., Maimí, P., & Mayugo, J. A. (2017). Modelling and simulation of tow-drop effects arising from the manufacturing of steered-fibre composites. *Composites Part A: Applied Science and Manufacturing*, *93*, 59–71.
Falcó, O., Mayugo, J. A., Lopes, C. S., Gascons, N., Turon, A., & Costa, J. (2014). Variable-stiffness composite panels: As-manufactured modeling and its influence on the failure behavior. *Composites Part B (Engineering)*, *56*, 660–669.
Fayazbakhsh, K., Nik, M. A., Pasini, D., & Lessard, L. (2013). Defect layer method to capture effect of gaps and overlaps in variable stiffness laminates made by Automated Fiber Placement. *Composite Structures*, *97*, 245–251.
Ghanem, R. G., & Spanos, P. D. (1991). *Stochastic finite elements: a spectral approach*. New York, New York, USA: Springer.
Gordon, W. J., & Hall, C. A. (1973). Transfinite element methods: Blending-function interpolation over arbitrary curved element domains. *Numerische Mathematik*, *21*, 109–129.
Hashin, Z., & Shtrikman, S. (1962). A variational approach to the theory of the elastic behaviour of polycrystals. *Journal of the Mechanics and Physics of Solids*, *10*(4), 343–352.
Hassani, B., & Hinton, E. (1998). A review of homogenization and topology optimization I—Homogenization theory for media with periodic structure. *Computers and Structures*, *69*(6), 707–717.
Heinrich, C., Aldridge, M., Wineman, A. S., Kieffer, J., Waas, A. M., & Shahwan, K. (2012). The influence of the representative volume element (RVE) size on the homogenized response of cured fiber composites. *Modelling and Simulation in Materials Science and Engineering*, *20*(7), Article 075007.
Hill, R. (1952). The elastic behaviour of a crystalline aggregate. *Proceedings of the Physical Society. Section A*, *65*(5), 349.
Kaleel, I., Carrera, E., & Petrolo, M. (2020). Progressive delamination of laminated composites via 1D models. *Composite Structures*, *235*, Article 111799.
Kaleel, I., Petrolo, M., Waas, A. M., & Carrera, E. (2017). Computationally efficient, high-fidelity micromechanics framework using refined 1D models. *Composite Structures*, *181*, 358–367.
Kaleel, I., Petrolo, M., Waas, A. M., & Carrera, E. (2018). Micromechanical progressive failure analysis of fiber-reinforced composite using refined beam models. *Journal of Applied Mechanics*, *85*(2).
Kirchhoff, G. (1850). Uber da gleichgewicht und die bewegung einer elastischen scheibe. *Journal Für Die Reine Und Angewandte Mathematik (Crelles Journal)*, *40*, 51–88.
Leissa, A. W., & Martin, A. F. (1990). Vibration and buckling of rectangular composite plates with variable fiber spacing. *Composite Structures*, *14*(4), 339–357.

Lekhnitskii, S. G. (1968). *Anisotropic plates*. New York, New York, USA: Gordon and Breach.
Llorca, J., González, C., Molina-Aldareguía, J. M., Segurado, J., Seltzer, R., Sket, F., et al. (2011). Multiscale modeling of composite materials: A roadmap towards virtual testing. *Advanced Materials*, *23*(44), 5130–5147.
Mindlin, R. D. (1951). Influence of rotary inertia and shear flexural motion of isotropic, elastic plates. *Journal of Applied Mechanics*, *18*, 31–38.
Mori, T., & Tanaka, K. (1973). Average stress in matrix and average elastic energy of materials with misfitting inclusions. *Acta Metallurgica*, *21*(5), 571–574.
Nemat-Nasser, S., & Hori, M. (2013). *Micromechanics: overall properties of heterogeneous materials*. Elsevier.
Pagani, A., Azzara, R., Augello, R., & Carrera, E. (2021). Stress states in highly flexible thin-walled composite structures by unified shell model. *American Institute of Aeronautics and Astronautics*, *59*(10), 4243–4256.
Pagani, A., Enea, M., & Carrera, E. (2021). Quasi-static fracture analysis by coupled three-dimensional peridynamics and high order one-dimensional finite elements based on local elasticity. *International Journal for Numerical Methods in Engineering*.
Pagani, A., de Miguel, A. G., Petrolo, M., & Carrera, E. (2016). Analysis of laminated beams via unified formulation and Legendre polynomial expansions. *Composite Structures*, *156*, 78–92.
Pagani, A., & Sanchez-Majano, A. R. (2020). Influence of fiber misalignments on buckling performance of variable stiffness composites using layerwise models and random fields. *Mechanics of Advanced Materials and Structures*, 1–16.
Pagani, A., & Sanchez-Majano, A. R. (2021). Stochastic stress analysis and failure onset of variable angle tow laminates affected by spatial fibre variations. *Composites Part C: Open Access*, *4*, Article 100091.
Pagani, A., Sanchez-Majano, A. R., & Zarate, I. S. (2021). Mechanical performance of variable stiffness plates subjected to multiscale defects. In *Proceedings of the American society for composites—thirty-sixth technical conference on composite materials*.
Pagani, A., Yan, Y., & Carrera, E. (2017). Exact solutions for static analysis of laminated, box and sandwich beams by refined layer-wise theory. *Composites Part B (Engineering)*, *131*, 62–75.
Poisson, S. D. (1829). Mémoire sur l'équilibre et le mouvement des corps élastiques. *Mémoires De L'académie Royal Des Sciences De L'institut De France*, *8*, 357–570.
Reddy, J. N. (1984). A simple higher-order theory for laminated composites. *Journal of Applied Mechanics*, *51*, 745–752.
Reddy, J. N., & Liu, C. F. (1985). A higher-order shear deformation theory of laminated elastic shells. *International Journal of Engineering Science*, *23*(3), 319–330.
Reissner, E. (1945). The effect of transverse shear deformation on the bending of elastic plates. *Journal of Applied Mechanics*, *12*(2), 69–77.
Sanchez-Majano, A. R., Azzara, R., Pagani, A., & Carrera, E. (2021). Accurate stress analysis of variable angle tow shells by high-order equivalent-single-layer and layer-wise finite element models. *Materials*, *14*(21), 6486.
Sanchez-Majano, A. R., Pagani, A., Petrolo, M., & Zhang, C. (2021). Buckling sensitivity of tow-steered plates subjected to multiscale defects by high-order finite elements and polynomial chaos expansion. *Materials*, *14*(11), Article 100091.
Scarth, C., & Adhikari, S. (2017). Modeling spatially varying uncertainty in composite structures using lamination parameters. *American Institute of Aeronautics and Astronautics*, *55*(11), 3951–3965.
Scarth, C., Adhikari, S., Cabral, P. H., Silva, G. HC, & do Prado, A. P. (2019). Random field simulation over curved surfaces: Applications to computational structural mechanics. *Computer Methods in Applied Mechanics and Engineering*, *345*, 283–301.
Smith, M. (2009). *ABAQUS/Standard user's manual, version 6.9*. United States: Dassault Systèmes Simulia Corp.
Sun, C. T., & Vaidya, R. S. (1996). Prediction of composite properties from a representative volume element. *Composites Science and Technology*, *56*(2), 171–179.
van den Broek, S., Minera, S., Jansen, E., & Rolfes, R. (2021). Robust improvement of the asymmetric post-buckling behavior of a composite panel by perturbing fiber paths. *Composite Structures*, *270*, Article 114011.
Viglietti, A., Zappino, E., & Carrera, E. (2019). Analysis of variable angle tow composites structures using variable kinematic models. *Composites Part B (Engineering)*, *171*, 272–283.
Yu, W. (2016). A unified theory for constitutive modeling of composites. *Journal of Mechanics of Materials and Structures*, *11*(4), 379–411.
Yu, W., Hodges, D. H., & Ho, J. C. (2012). Variational asymptotic beam sectional analysis–An updated version. *International Journal of Engineering Science*, *59*, 40–64.
Yu, W., & Tang, T. (2007). A variational asymptotic micromechanics model for predicting thermoelastic properties oh heterogeneous materials. *International Journal of Solds and Structures*, *44*, 7510–7525.
Zhao, Z., Dang, H., Zhang, C., Yun, G. J., & Li, Y. (2018). A multi-scale modeling framework for impact damage simulation of triaxially braided composites. *Composites Part A: Applied Science and Manufacturing*, *110*, 113–125.